

RESEARCH ARTICLE

Generation and Stress Analysis of Helical Gear Tooth Combining Involute with Epicycloidal and Hypocycloidal Profiles

Mohammed Abdulaal Kadhim*, Mohammad Qasim Abdulah

Mechanical Engineering Department, College of Engineering, University of Baghdad, Iraq

ABSTRACT – This paper examines the helical gear that combines the involute with epicycloidal-hypocycloidal profiles. The tooth profile was produced through the shaper-cutting process, which was conducted using an appropriate rack cutter with a Cartesian coordinate system. A computer program was developed using Microsoft Visual Basic and subsequently integrated into SolidWorks using the application programming interface. This numerical investigation aims to analyze the impact of tool parameters on the produced gear tooth profile, with the goal of enhancing the dynamic performance and deformation resistance of the proposed helical gear model. Additionally, this study assesses the effect of teeth thickness on the helical gear model. The results indicate a highly accurate approximation of the involute, cycloidal, and modified gear tooth profiles, which were programmed according to the module, teeth number, and rolling angle. The use of a combination of curves (epicycloidal, involute, and hypocycloidal) in a single tooth resulted in a larger contact area, thereby improving the ability of the gears to withstand greater pressures and extending their lifespan. The modified non-parallel helical gear drive outperformed other non-parallel helical gear drives. The best enhancements in maximum contact stress and teeth bending stress achieved approximately 33.169% and 26.08% compared to the standard involute profile and about 17.69% and 0.67% when compared to the cycloidal profile.

ARTICLE HISTORY

Received : 25th Dec. 2023

Revised : 30th Dec. 2024

Accepted : 24th Jan. 2025

Published : 20th Feb. 2025

KEYWORDS

Helical gear

Generating process

Involute

Cycloidal

Epicycloidal

Hypocycloidal

1. INTRODUCTION

The primary failure mechanisms associated with helical gear drives during mutual contact are diverse. Gears typically experience two fundamental forms of tooth failure: fracture due to static and dynamic loads, as well as profile degradation, which can be attributed to the misalignment of the teeth pair during engagement, leading to interference between the edges of the gear teeth. A period of overlap exists in which two pairs of profiles are simultaneously in contact. Surface destruction, or tooth wear, can be categorized into five types based on its principal causes: abrasive wear, corrosive wear, early pitting, destructive pitting, and excessive scoring. This type of failure is characterized by the presence of pits that progressively enlarge, compromising the tooth surface and, in some cases, resulting in premature tooth fracture. Gear teeth may fail due to surface fatigue if the applied load exceeds the material's surface endurance strength. Bending failure occurs when the contact force on the tooth reaches or exceeds the yield strength of the gear tooth material. Modifications to gear design characteristics may prevent the tooth from breaking completely. Non-conventional helical teeth are used to minimize contact stress and improve tooth deflection and root stress. This study aims to systematically reduce contact stress, improve tooth deflection and root stress, and address interference effectively.

Despite extensive research on contact and bending stresses in non-parallel helical gear drives, there are still concerns regarding this topic. Oswald [1] investigated the impact of contact area on noise generation in gearboxes with various tooth profiles of conventional and double helical gears, including two curves (i.e., involute and circular arc). The findings indicate that the contact ratio influences noise production across different gear variants. Litvin et al. [2] examined contact and bending stresses with transmission faults in typical involute teeth of spur gears influenced by two modifications: pressure angle and double crowning of teeth. An increase in pressure angle was found to enhance contact stresses for both symmetric and asymmetric teeth while reducing transmission errors for crowned teeth. Kumar [3] analyzed the cycloid spur gear profile and the impact of tooth count, module, and roller radius on bending and contact stresses and compared the findings with the involute tooth profile. The results indicate that the root stress of cycloid gears surpasses that of involute teeth under identical parameters. An increase in the module and a decrease in the number of teeth were shown to reduce bending stress, while the involute tooth profile produced less noise compared to the cycloidal tooth profile.

Cananau [4] utilized the finite element method in ANSYS software to analyze tooth contact and root stresses of the involute gear tooth profile along the contact line during the tooth meshing cycle. The results indicate that the contact stress distribution in the front plane of the gear model corresponds to the root stress in the tooth fillet area along the contact line, with a significant escalation of stress on the tooth root fillet under non-uniform contact conditions during the meshing process. Kapelevich [5] investigated the mathematical formulation of standard and non-standard involute teeth for spur gears and examined the bending stress in the root fillet and the reduction of stress concentration on the gear tooth surface. The study demonstrated that non-standard gear teeth increased the bending strength by approximately 33% and

*CORRESPONDING AUTHOR | Mohammed Abdulaal Kadhim | ✉ mohammed.abd2103p@coeng.uobaghdad.edu.iq

reduced the contact stress by around 20%. Farhangdoost et al. [6] conducted an analytical and numerical analysis of contact stress in conventional spur gears influenced by various geometric design elements. Four distinct examples of contact stress (involute, cycloidal, epicycloidal, and hypocycloidal) were compared. The results indicate that, in comparison to involute teeth, the decrease in contact stress for the same design is 30% for cycloidal, 46% for epicycloidal, and 21% for hypocycloidal profiles. Abdullah [7] presented an analytical solution using a trial graphical method to calculate the bending strength for asymmetric involute spur gear teeth, which was subsequently modified by Abdullah and Kadum [8] for calculating the bending strength for asymmetric involute helical gears. This equation can be utilized for symmetric helical gear teeth with a standard pressure angle (14.5°), asymmetric helical gear teeth with a pressure angle of 14.5° at the right side, and different pressure angles at the left side, varying from 20° to 35° in each step of 5° .

Miltenović and Banić [9] explored the technical challenges and service landscape of high-strength gears, proposing a rapid methodology for forecasting the temperature of the gearbox system via finite element analysis (FEA). The gearbox was designed to calculate the ambient temperature of the gear unit for thermal stability determination. This methodology was developed to enable gear system designers to perform rapid FEA computation for temperature assessment. Gear designers use non-standard tooth profiles rather than traditional standard teeth. Consequently, the bending strength is enhanced by reaching the apex of the tooth. Becker et al. [10] established a parallel rack profile using a fourth-order polynomial. The design enhanced flank geometries and their characteristics were examined. A composite of steel worms and plastic wheels was engineered to replace several steel applications with highly efficient plastic materials, thereby improving the efficiency and strength of crossed helical gears. The study examined deformation and load distribution in different engagements based on dominant load and plastic material stiffness. The assumptions used in the computation provide strong concordance in both methodologies. The geometries of the two wheels were obtained by meshing each wheel with one side of the rack, allowing both wheels to intermesh while accounting for shaft angles deviating from 90° . This computation is also applicable to spur gears.

Wu et al. [11] devised innovative flank shapes and modifications for crossed helical gears to enhance their efficiency. The study summarizes technical difficulties in transmission design, materials and manufacturing, design and manufacturing integration, and processing and performance assessment of high-strength gears. The study also discusses common applications in engineering equipment, wind power generation, and aviation engines, while highlighting recent advancements in anti-fatigue design, manufacture, and service performance assessment of high-strength gears. The objective of the study is to encourage the development and use of high-strength gear technology. In general, gears are used to transmit motion and power across shafts at various skew angles in numerous mechanical applications. The gearing system is regarded as an ideal drive in many applications [12]. Consequently, toothed gearing is a crucial component in gearbox transmission, offering several advantages, including a consistent speed ratio in the absence of slippage, extended service life, excellent dependability, and compact dimensions [13]. Three types of cases used for power transmission include involute, circular arc, and cycloid. The convex flank of one cycloidal tooth contacts the concave flank of the corresponding tooth, resulting in an extensive contact area that enhances wear resistance [14]. The contact in the involute gear profile occurs between two convex surfaces on interfacing teeth, resulting in a reduced contact area and less wear resistance [15].

By combining knowledge with that of past researchers, previous surveys have provided convincing alternatives that enhance the load-carrying capacity of gears. More studies are being conducted on gearing technology systems to address the growing demand for improved dynamic gear drive performance. In this work, the present tooth is different from previous studies, where the unique tooth profile is analyzed to evaluate the contact with the root stress region numerically and compare it with the standard gear involute and cycloid tooth. Therefore, it is crucial to identify methods that enhance the characteristics of the tooth profile through the integration of two curves, specifically the amalgamation of involute profiles with epicycloidal and hypocycloidal profiles. The integrated tooth shape is designed to reduce bending loads, contact stresses, and tooth deflection, thereby preventing pinion failure inside the gearbox [16], [17]. Various techniques exist for the production of involute and cycloidal gears. To accurately produce the gear tooth profile or manufacture the gear using a standard CNC milling machine without form cutters, it is essential to determine the coordinates of the tooth profile corresponding to a specific production rack. This study will demonstrate the shaping process utilizing a cutting tool.

2. COORDINATE SYSTEM

Calculating the coordinates for locations on the gear contact surface is rather straightforward. The operation can be performed directly if the geometry of the rack used to produce the combined gear tooth profile is analytically comprehended. However, this method, which is complex to implement, requires data regarding the tooth profile, including a description of the rack, such as the module, teeth number, pressure angle, rolling angle, radius of generation, and helix angle. This study employs two coordinate transformations based on the fourth-order application of rotational and translational matrices. The first coordinate system illustrates the translation-rotation movements, whereas the subsequent one depicts the rotational motion between two wheels [18].

The first transformation is represented by coordinate systems. S_g and S_r are firmly affixed to the wheel and the trapezoidal rack cutter, respectively. The performance of rotational and translational movements is relative to a fixed point at the origin in the global system of coordinate S_f , as seen in Figure 1. Point M is located inside the coordinate

system S_g . The position vector is defined as $S_g = \overline{O_g M}$. Changes to the coordinates from S_g to S_r are defined by the matrix transformation M_{r_g} . The coordinate transformation from the first point on S_g to the second point on S_r is based on the matrix transformation.

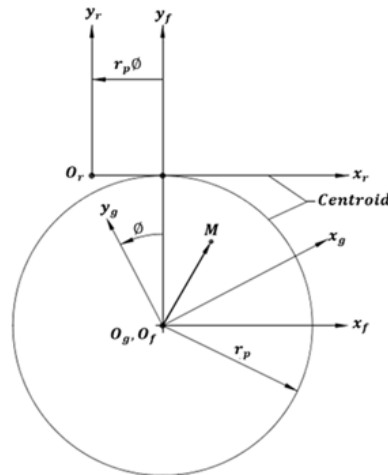


Figure 1. System for the coordination of translation and rotation

$$r_r = M_{r_g} r_g = M_{r_f} M_{f_g} r_g \tag{1}$$

where M_{r_f} denotes the translational matrix and M_{f_g} is the rotational matrix that denotes the state of rotation around the z_f axis.

The rotation from S_g to S_r occurs in a clockwise direction. In this context, the unit vector C_f is defined as follows:

$$c_f = [0 \ 0 \ 1]^T \tag{2}$$

The following matrix is obtained by rotating the coordinate system from S_g to S_r clockwise, while ensuring that the two elements of the vector of unit are equivalent to zero and $C_f = k_f$.

$$M_{f_g} = \begin{bmatrix} \cos\phi & -\sin\phi & 0 & 0 \\ \sin\phi & \cos\phi & 0 & 0 \\ 0 & 0 & 1 & 0 \\ 0 & 0 & 0 & 1 \end{bmatrix} \tag{3}$$

Figure 1 indicates that:

$$(\overline{O_r O_f})_f = [r_p \phi \ -r_p \ 0]^T \tag{4}$$

The translational matrix can be calculated using the following formula:

$$M_{r_f} = \begin{bmatrix} 1 & 0 & 0 & r_p \phi \\ 0 & 1 & 0 & -r_p \\ 0 & 0 & 1 & 0 \\ 0 & 0 & 0 & 1 \end{bmatrix} \tag{5}$$

The vectors \vec{r}_g and \vec{r}_r are positioned as follows:

$$\vec{r}_g = [x_g i \ y_g j \ z_g k \ 1]^T, \vec{r}_r = [x_r i \ y_r j \ z_r k \ 1]^T \tag{6}$$

The transformation matrix derived from Equations 1–6 is as follows:

$$M_{r_g} = \begin{bmatrix} \cos\phi & -\sin\phi & 0 & r_p \phi \\ \sin\phi & \cos\phi & 0 & -r_p \\ 0 & 0 & 1 & 0 \\ 0 & 0 & 0 & 1 \end{bmatrix} \tag{7}$$

$$x_r = x_g \cos\phi - y_g \sin\phi + r_p \phi \tag{8}$$

$$y_r = x_g \sin\phi + y_g \cos\phi - r_p \tag{9}$$

$$z_r = z_g \tag{10}$$

In order to ascertain the location \vec{r}_g in relation to the position \vec{r}_r , the inverse matrix $M_{r_g}^{-1} = M_{g_r}$ is determined in relation to the elements of matrix M_{r_g} . However, M_{r_g} is not unique; thus, the inverse of this matrix is feasible. Therefore:

$$M_{gr} = \begin{bmatrix} \cos\phi & \sin\phi & 0 & r_p(\sin\phi - \phi\cos\phi) \\ -\sin\phi & \cos\phi & 0 & r_p(\cos\phi + \phi\sin\phi) \\ 0 & 0 & 1 & 0 \\ 0 & 0 & 0 & 1 \end{bmatrix} \tag{11}$$

Subsequently, the matrix can be utilized as:

$$r_g = M_{gr}r_r \tag{12}$$

Following that:

$$x_g = x_r\cos\phi + y_r\sin\phi + r_p(\sin\phi - \phi\cos\phi) \tag{13}$$

$$y_g = -x_r\sin\phi + y_r\cos\phi + r_p(\cos\phi + \phi\sin\phi) \tag{14}$$

$$z_g = z_r \tag{15}$$

The second transformation is represented by two types. The first transformation is coordinate systems $S_p(x_p, y_p, z_p)$ and $S_g(x_g, y_g, z_g)$ that are securely linked to the two wheels, denoted as g and p , respectively. The rotational change will occur around parallel axes. ϕ_p and ϕ_g represent the rotation angles for the two wheels, respectively, as seen in Figure 2. These angles are connected by the following equation:

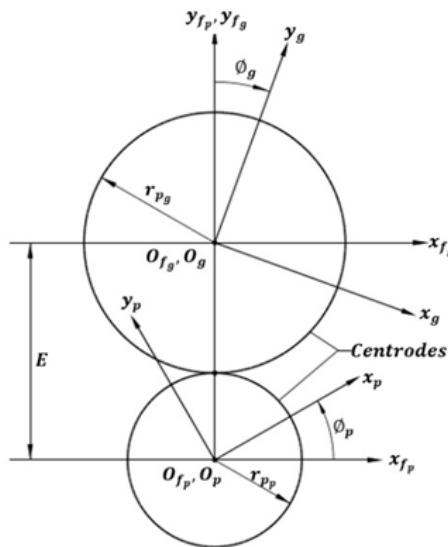


Figure 2. Coordinate system of rotational motion in opposite direction

$$\frac{\phi_g}{\phi_p} = \frac{r_{pg}}{r_{pg}} \tag{16}$$

The terms r_{pg} and r_{pg} are the pinion's and the gear's pitch circle radii, respectively, while E represents the minimal distance between the rotational axis. S_{fp} and S_{fg} are auxiliary coordinate systems that are securely affixed to the fixed frame for each pinion and gear cylinder. The coordinate transformation system transitioning from S_g to S_p is based on the following matrix:

$$r_p = M_{pg}r_g = M_{pfp}M_{fpfg}M_{fpg}r_g \tag{17}$$

M_{pfp} and M_{fpg} represent the rotating matrix, whereas M_{fpfg} denotes the translational matrix.

Therefore:

$$r_p = [x_p \quad y_p \quad z_p \quad 1]^T \tag{18}$$

$$r_g = [x_g \quad y_g \quad z_g \quad 1]^T \tag{19}$$

$$M_{fpg} = \begin{bmatrix} \cos\phi_g & \sin\phi_g & 0 & 0 \\ -\sin\phi_g & \cos\phi_g & 0 & 0 \\ 0 & 0 & 1 & 0 \\ 0 & 0 & 0 & 1 \end{bmatrix} \tag{20}$$

$$M_{pf_p} = \begin{bmatrix} \cos\phi_p & \sin\phi_p & 0 & 0 \\ -\sin\phi_p & \cos\phi_p & 0 & 0 \\ 0 & 0 & 1 & 0 \\ 0 & 0 & 0 & 1 \end{bmatrix} \tag{21}$$

$$M_{f_p f_g} = \begin{bmatrix} 1 & 0 & 0 & 0 \\ 0 & 1 & 0 & E \\ 0 & 0 & 1 & 0 \\ 0 & 0 & 0 & 1 \end{bmatrix} \tag{22}$$

The equation yields the following matrix:

$$M_{pg} = \begin{bmatrix} \cos(\phi_p + \phi_g) & \sin(\phi_p + \phi_g) & 0 & E\sin\phi_p \\ -\sin(\phi_p + \phi_g) & \cos(\phi_p + \phi_g) & 0 & E\cos\phi_p \\ 0 & 0 & 1 & 0 \\ 0 & 0 & 0 & 1 \end{bmatrix} \tag{23}$$

Equations 17–23 are used to produce the following equations:

$$x_p = x_g \cos(\phi_p + \phi_g) + y_g \sin(\phi_p + \phi_g) + E\sin\phi_p \tag{24}$$

$$y_p = -x_g \sin(\phi_p + \phi_g) + y_2 \cos(\phi_p + \phi_g) + E\cos\phi_p \tag{25}$$

$$z_p = z_g \tag{26}$$

In order to obtain the components of the matrix M_{gp} , the inverse matrix M_{pg}^{-1} is utilized:

$$M_{gp} = \begin{bmatrix} \cos(\phi_p + \phi_g) & -\sin(\phi_p + \phi_g) & 0 & E\sin\phi_g \\ \sin(\phi_p + \phi_g) & \cos(\phi_p + \phi_g) & 0 & -E\cos\phi_g \\ 0 & 0 & 1 & 0 \\ 0 & 0 & 0 & 1 \end{bmatrix} \tag{27}$$

The transformation of inverse coordinates is defined by the following matrix equation:

$$r_g = M_{gp}r_p \tag{28}$$

Equation 28 resulted in:

$$x_g = x_p \cos(\phi_p + \phi_g) - y_p \sin(\phi_p + \phi_g) + E\sin\phi_g \tag{29}$$

$$y_g = -x_p \sin(\phi_p + \phi_g) + y_p \cos(\phi_p + \phi_g) - E\cos\phi_g \tag{30}$$

$$z_g = z_p \tag{31}$$

For the second transformation, two gears convert the rotation along parallel axes while maintaining the same directional orientation, as seen in Figure 3. The coordinate systems $S_p(x_p, y_p, z_p)$ and $S_g(x_g, y_g, z_g)$ are securely affixed to the two wheels. S_{f_p} and S_{f_g} are established coordinate systems; E represents the minimal distance between the rotation axes; ϕ_p and ϕ_g represent the rotation angles for the two wheels, respectively; and r_{p_p} and r_{p_g} are wheel 1's and wheel 2's radii of the pitch circles, respectively.

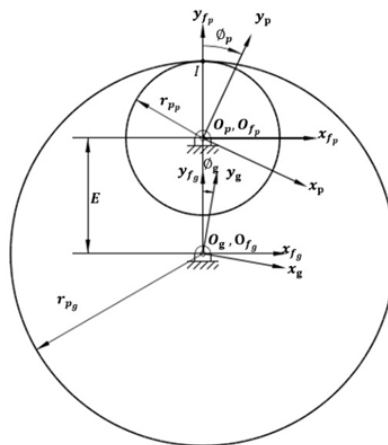


Figure 3. Coordinate system of rotational motion in the same direction

The transformation matrix M_{gp} is as follows:

$$M_{gp} = M_{gf_g} M_{f_g f_p} M_{f_p p} \quad (32)$$

$$M_{gp} = \begin{bmatrix} \cos(\phi_p - \phi_g) & \sin(\phi_p - \phi_g) & 0 & -E \sin \phi_g \\ -\sin(\phi_p - \phi_g) & \cos(\phi_p - \phi_g) & 0 & E \cos \phi_g \\ 0 & 0 & 1 & 0 \\ 0 & 0 & 0 & 1 \end{bmatrix} \quad (33)$$

The inverse matrix $M_{gp} = M_{gp}^{-1}$:

$$M_{pg} = \begin{bmatrix} \cos(\phi_p - \phi_g) & -\sin(\phi_p - \phi_g) & 0 & E \sin \phi_p \\ \sin(\phi_p - \phi_g) & \cos(\phi_p - \phi_g) & 0 & -E \cos \phi_p \\ 0 & 0 & 1 & 0 \\ 0 & 0 & 0 & 1 \end{bmatrix} \quad (34)$$

As a result, the coordinate transformation from s_p to s_g is as follows:

$$x_g = x_p \cos(\phi_p - \phi_g) + y_p \sin(\phi_p - \phi_g) - E \sin \phi_g \quad (35)$$

$$y_g = -x_p \sin(\phi_p - \phi_g) + y_p \cos(\phi_p - \phi_g) + E \cos \phi_g \quad (36)$$

$$z_g = z_p \quad (37)$$

Subsequently, the coordinate transformation from s_g to s_p is as follows:

$$x_p = x_g \cos(\phi_p - \phi_g) - y_g \sin(\phi_p - \phi_g) + E \sin \phi_p \quad (38)$$

$$y_p = -x_g \sin(\phi_p - \phi_g) + y_2 \cos(\phi_p - \phi_g) - E \cos \phi_p \quad (39)$$

$$z_p = z_g \quad (40)$$

3. GENERATION OF GEAR TOOTH PROFILE

The gear tooth profile can be represented by curves and surfaces derived using the coordinate transformation approach. A point that follows a predetermined path produces the assumed curve. Furthermore, the surface is created by a curve that follows a certain trajectory [19].

3.1 Generation of Involute Curve

An involute curve is produced by a certain point M that is firmly attached to the line \overline{BD} . This straight line rotates without sliding across the circle with a radius of ρ , as illustrated in Figure 4. The derivation of the involute curve relies on Equations 11, 12, and 13, which delineate the coordinate transformation from S_r to S_g . The creating point is denoted in the system of coordinate S_g by:

$$\begin{bmatrix} x_g^{(M)} & y_g^{(M)} & z_g^{(M)} & 1 \end{bmatrix}^T = \begin{bmatrix} 0 & -a & 0 & 1 \end{bmatrix}^T \quad (41)$$

Where a is constant.

The approach yields the following equations of the involute curve:

$$x_g = -a \sin \phi + \rho (\sin \phi - \phi \cos \phi) \quad (42)$$

$$y_g = -a \cos \phi + \rho (\cos \phi + \phi \sin \phi) \quad (43)$$

Equations 42 and 43 indicate that there are two categories of involute curves. An ordinary involute curve is produced when $a = 0$. Conversely, a shortened involute curve is generated if $y_2^{(M)} = a > 0$. Figure 4 illustrates the involute curve utilized to construct a tooth surface.

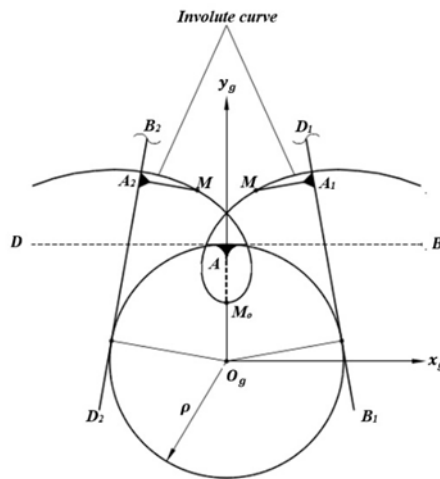


Figure 4. Generation of the involute curve

3.2 Generation of Cycloid Curve

A cycloid curve is produced by a point M that is firmly attached to a radius circle γ . This circle rolls down a straight line without sliding, as seen in Figure 5. The system of coordinate S_g is firmly enclosed in the circle. The coordinate system S_r is strictly linked to the linear path. The creating point is delineated in the system of coordinate S_r by:

$$\overline{O_r M} = [0 \quad -a \quad 0 \quad 1]^T \tag{44}$$

The coordinate of transformation in the transition matrix from S_r to S_g is delineated by the following equations [18]:

$$x_g = -a \sin\phi + \gamma\phi \tag{45}$$

$$y_g = a \cos\phi - \gamma \tag{46}$$

An ordinary cycloid is generated when $a = \gamma$, while a shorter cycloid is generated when $a < \gamma$.

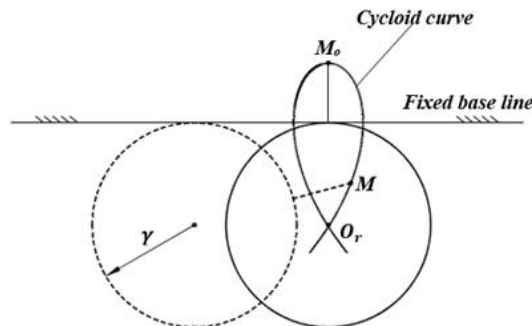


Figure 5. Generation of the cycloid curve

3.3 Generation of Epicycloid and Hypocycloid Curves

An epicycloid curve is produced by a point M that is securely attached to circle 2. This circle rolls without sliding over the externally tangent circle 1. The radii of the circles are γ_1 and γ_2 . They possess centred, and the relative motion between them is characterized by pure rolling. Figure 6 depicts the curve formed by the coordinate system S_p . M_0 and M denote two locations of the point of tracking for the epicycloid curve. The epicycloid is delineated in the system of coordinate S_p that is permanently affixed to circle 1. The equations of the epicycloid curve can be determined through coordinate transformation from S_g to S_p , as shown in Figure 6. The generation point M is delineated inside the coordinate system S_g by:

$$\begin{bmatrix} x_g^{(M)} & y_g^{(M)} & z_g^{(M)} & 1 \end{bmatrix}^T = [0 \quad -a \quad 0 \quad 1]^T \tag{47}$$

Where $a = O_2M > \gamma_2$.

Integrating Equations 29, 30, and 31 into Equation 47 produces the following equations:

$$x_p = (\gamma_1 + \gamma_2)\sin\phi_1 - a \sin \left[\phi_1 \left(1 + \frac{\gamma_1}{\gamma_2} \right) \right] \tag{48}$$

$$y_p = (\gamma_1 + \gamma_2)\cos\phi_1 - a \cos\left[\phi_1\left(1 + \frac{\gamma_1}{\gamma_2}\right)\right] \tag{49}$$

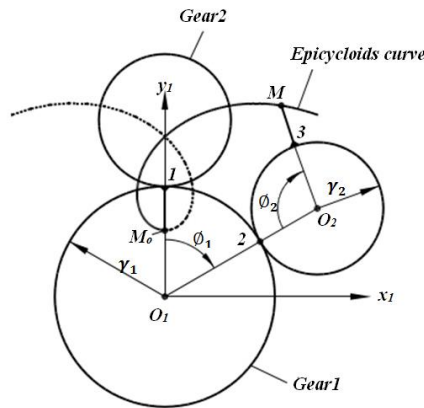


Figure 6. Generation of the epicycloid curve

The derivations of the hypocycloid curve are based on an alternate methodology similar to the prior process. The generating circle 2 will rotate inside circle 1 in the same manner, as illustrated in Figure 7. Consequently, the computations use $(\gamma_1 - \gamma_2)$ rather than $(\gamma_1 + \gamma_2)$ in the aforementioned equations. The subsequent modified equations of the hypocycloid curve are:

$$x_p = (\gamma_1 - \gamma_2)\sin\phi_1 - a \sin\left[\phi_1\left(\frac{\gamma_1}{\gamma_2} - 1\right)\right] \tag{50}$$

$$y_p = (\gamma_1 - 1)\cos\phi_1 + a \cos\left[\phi_1\left(\frac{\gamma_1}{\gamma_2} - 1\right)\right] \tag{51}$$

For a standard epicycloid and hypocycloid, the constant a will be equal to γ_1 .

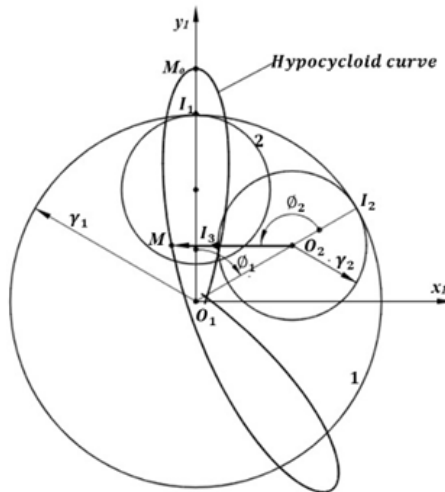


Figure 7. Generation of the hypocycloid curve

4. GENERATION OF GEAR TOOTH PROFILE USING TOOLS

The cross-section of the gear tooth surface is generated at the plane. Figure 8 illustrates the position of the cutter to the wheel for cutting. The relationship between the angular velocity w of the rotating gear blank around point O , measured in rpm, and the velocity of the translational cutter v , expressed in mm/sec, is given by [20]:

$$\frac{|v|}{w} = r_p = \frac{z}{2D_p} \tag{52}$$

In this context, r_p denotes the pitch circle radius, Z represents the teeth number, and D_p signifies the diametral pitch. The circle of the pitch can be regarded as the wheel centred formed by cutting. The cutter has a pitch line, which is an imperceptible straight line perpendicular to the circle of the pitch and parallel to the linear velocity direction. Throughout the cutting procedure, the rack oscillates parallel to the gear rotation axis. The gear tooth configuration is produced as the envelope for the set of rack-cutter profiles [21].

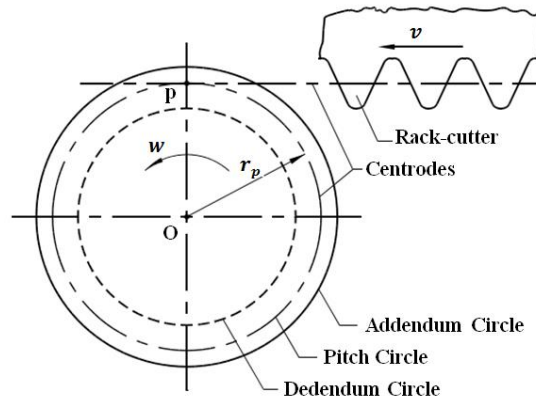


Figure 8. Generation of tooth profile using a rack-cutter

In this work, several rack-cutter shapes were used to generate different types of gear tooth profiles. Figure 9 shows the cutters used to generate different samples of gear teeth, including the trapezoid cutter, cycloid cutter, and modified cutter (non-standard). Figures 9(c) and (d) show the modified rack-cutters for mixed tooth profile gears that consist of a straight line and a cycloid curve.

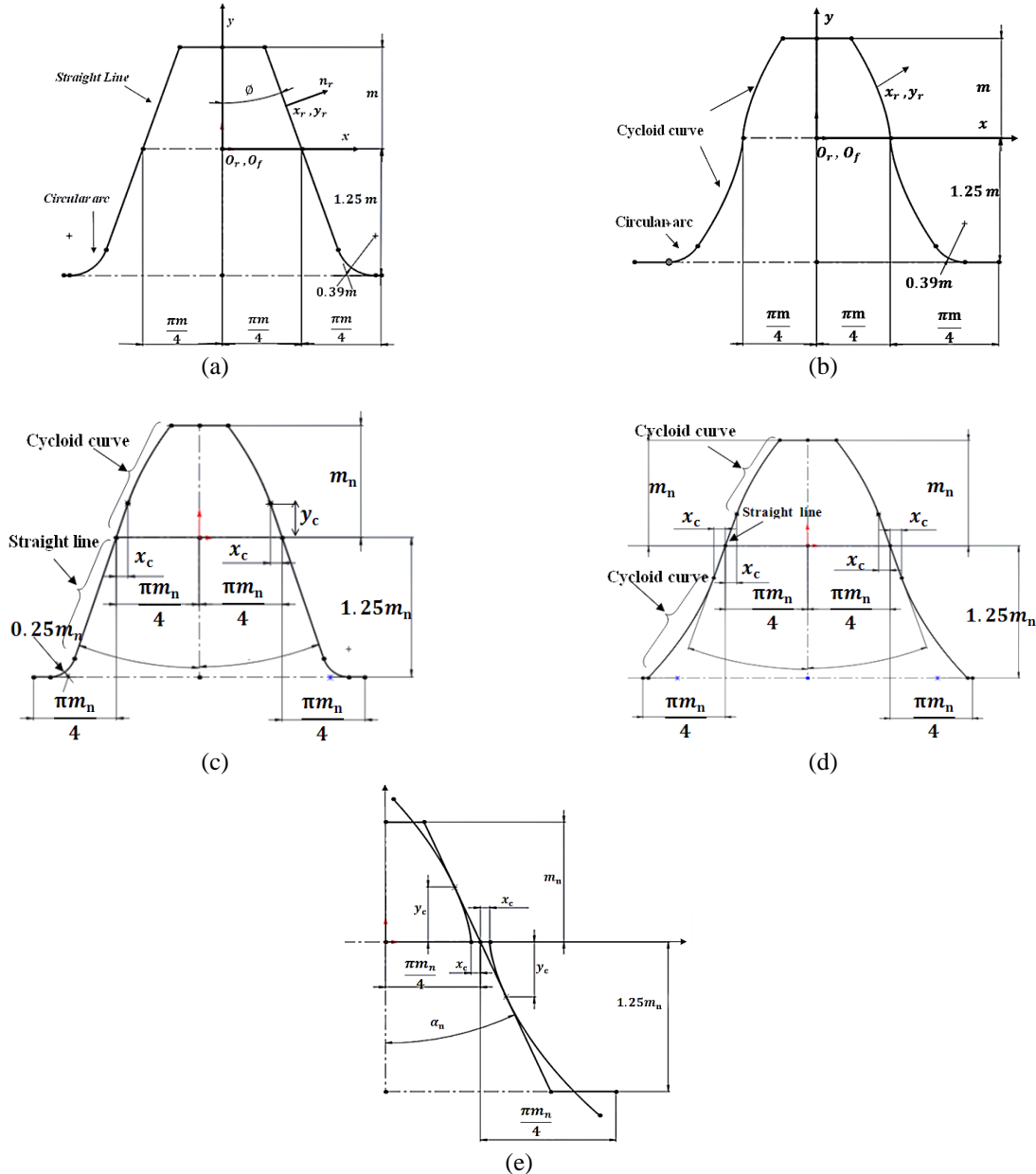


Figure 9. Coordinate systems of rack-cutters for the (a) trapezoid cutter, (b) cycloid cutter, (c) modified cutter 1, and (d) modified cutter 2, and (e) the cycloid curve coordinate system with a straight line

The equation of a straight line can be expressed using the coordinate system, as indicated in the equation [20].

$$x_r = y_r \tan(\alpha) \tag{53}$$

The coordinate system for the cycloid curve is defined by Equations 45 and 46. The initial coordinates of the cycloid curve are defined as x_c along the X-axis and y_c along the Y-axis, as shown in Figure 9(e). These coordinates can be determined using the following calculations [14], [22]:

$$x_c = 2R \sin(\alpha) \tag{54}$$

$$y_c = R - R \cos(2\alpha) \tag{55}$$

Where α is the inclination of a straight line to the Y-axis, which is equivalent to the cutter pressure angle of the involute curve, R is the rolling circle radius, and x_c and y_c are the distance between the pitch point and the cycloid curve begins.

Subsequently, the procedures for the creation of a helical gear are finalized by designing the parameter of the helix angle on the pitch cylinder. The helicoid surface is formed by a set of planar curves of identical shape executing a helical motion [21]. Figure 10 illustrates two coordinate systems. The first S_o is a fixed coordinate and the second S_h is a movable coordinate system that executes a helical motion regarding S_o . In this context, the axial displacement and rotation angle in helical motion are defined by ψ and $p\psi$, respectively, where p is the helical motion parameter or “the pitch of the helical,” which is provided by [23]:

$$p = \frac{H}{2\pi} \tag{56}$$

The axial displacement H is associated with a single full rotation.

The planar curve L is defined in a system of coordinates $S_h(x_h, y_h, z_h)$, as shown in Figure 10, by the following equation [24]:

$$x_h = x_h(\theta), y_h = y_h(\theta), z_h = 0 \quad \theta_1 \leq \theta \leq \theta_2 \tag{57}$$

Where θ is an independent variable. The created helicoid surface is defined in the system of coordinates; therefore, the equation becomes:

$$r_o = M_{oh} r_h \tag{58}$$

Where:

$$r_o = [x_o \quad y_o \quad z_o \quad 1]^T \tag{59}$$

$$r_h = [x_h(\theta) \quad y_h(\theta) \quad z_h(\theta) \quad 1]^T \tag{60}$$

$$M_{oh} = \begin{bmatrix} \cos\psi & -\sin\psi & 0 & 0 \\ \sin\psi & \cos\psi & 0 & 0 \\ 0 & 0 & 1 & p\psi \\ 0 & 0 & 0 & 1 \end{bmatrix} \tag{61}$$

Using the matrix equation in Equation 58 yields:

$$x_o = x_h(\theta) \cos\psi - y_h(\theta) \sin\psi \tag{62}$$

$$y_o = x_h(\theta) \sin\psi + y_h(\theta) \cos\psi \tag{63}$$

$$z_o = p\psi \tag{64}$$

Where $\theta_1 \leq \theta \leq \theta_2$ and $\psi_1 \leq \psi \leq \psi_2$.

Equations 62, 63, and 64 represent the generated helicoid surface. The surface coordinates are specified by the given values at any x_o , y_o , and z_o positions, which are defined by θ and ψ .

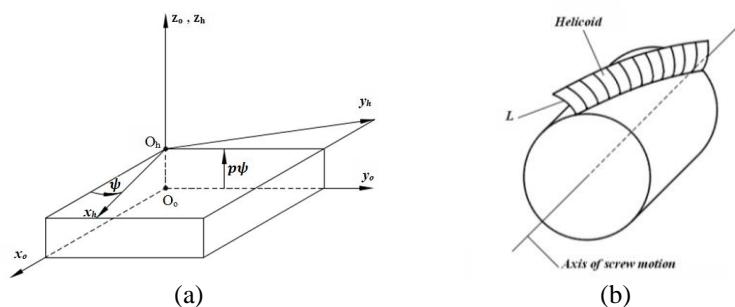


Figure 10. Generation of the helicoid: (a) illustration of the coordinate system and (b) illustration of the generation of a helicoid by screw motion

5. SOFTWARE PROGRAM

The computer software is based on the equations outlined in the previous section for the creation of involute, cycloidal, and modified helical gear tooth profiles. The software was written using Microsoft Visual Basic and subsequently integrated with the programming interface of SolidWorks using macro recording. The essential input data are the normal module, normal pressure angle, helix angle, teeth number, addendum circle radius, rolling radius, rotation angle, screw parameter, and face width. The methodology employed by the program is illustrated in a schematic diagram in Figure 11. The following section elucidates the processes involved in tooth creation and the methods for creating various surfaces of compounded curves [25].

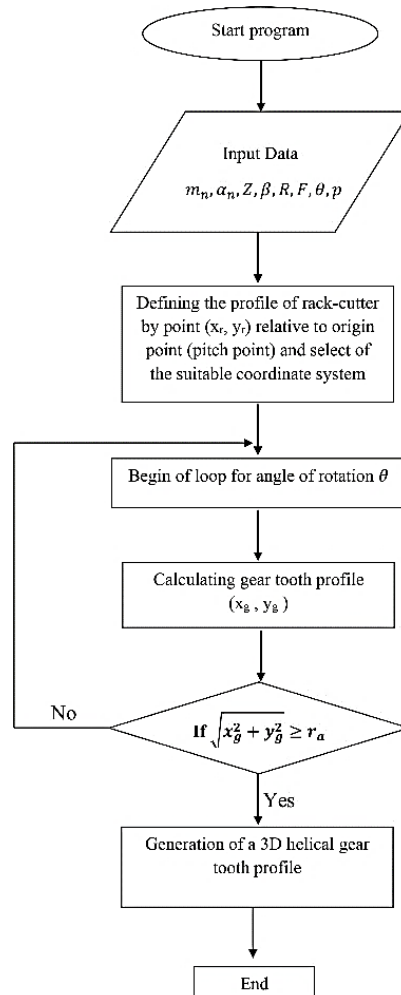


Figure 11. Flow chart of generation of tooth profile for different curve helical gear

6. RESULTS AND DISCUSSION

At the stress concentration location at the gear teeth root, bending stress is a major contributor to tooth failure. The system is brought to a halt by this catastrophic disaster. The objective of this project is to investigate the effect of the teeth profile design on the thickness of the gear teeth base to increase its strength resistance. Figures 12 and 13 provide the fundamental findings of the program and illustrate the family of forms for trapezoid and cycloid cutters, as well as the final tooth profiles of the produced gears. The results of the simulation indicate that the teeth of the produced gears act as cantilevered beams [26], with the cross-sectional area and tooth thickness that are directly related to the distance between the normal load position and the maximum stress zone. This study seeks to identify the weakest tooth thickness among various tooth systems that affect gear bending strength.

The configuration of the rack cutters, in conjunction with the coordinate system employed in this analysis, is crucial for accurately depicting the gear teeth. The initial coordinate system, which involves the translation and rotation between a line and a circle, utilizes the trapezoidal cutter. This system is characterized by a straight line that produces the involute curve of the gear teeth surface, as illustrated in Figure 12. The second coordinate system involves rotational motion between two circles and employs a cycloid cutter composed of two cycloid curves. These curves produce the epicycloid and hypocycloid shapes that define the surface of the gear teeth, as illustrated in Figure 13. A shaper may use the modified rack cutter to form the contour of the gear teeth. This cutter consists of a straight line at its center, two upper and lower cycloid curves, and an additional area. Consequently, the tooth gear may exhibit an epicycloidal, involute, and hypocycloidal configuration, respectively.

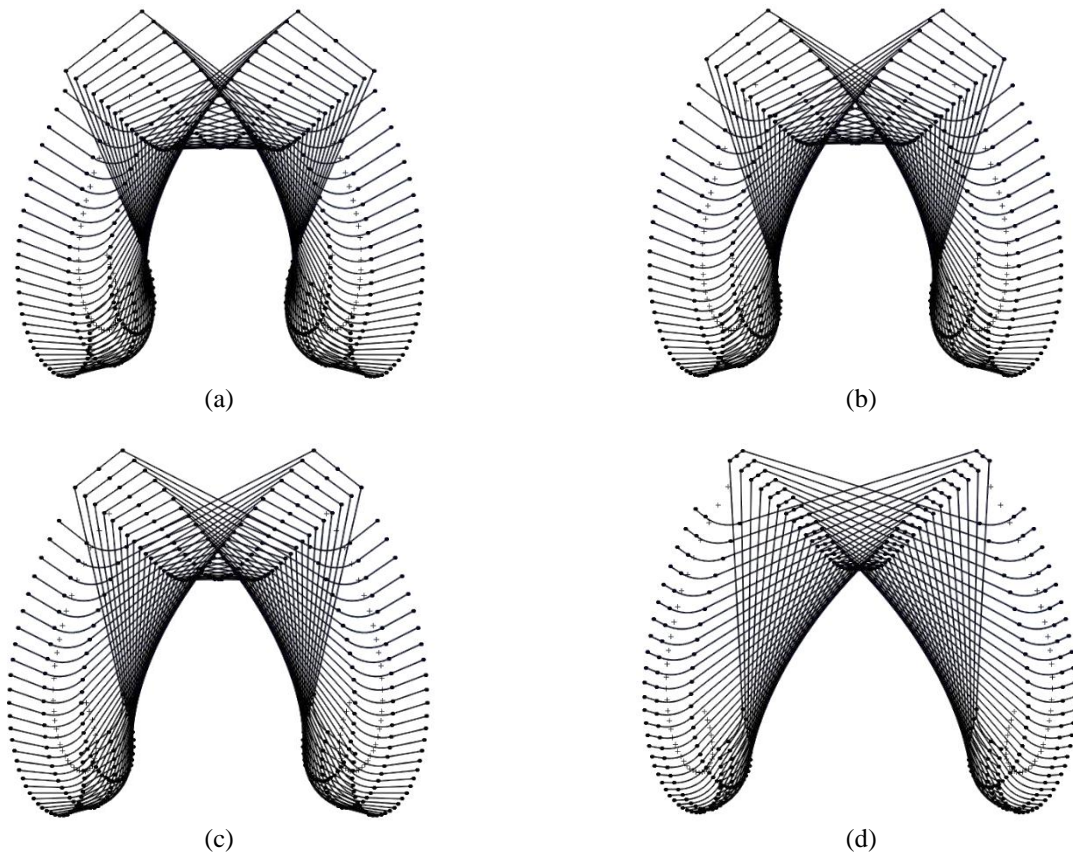


Figure 12. Involute tooth geometry for 14 teeth: (a) $\alpha_n = 14.5^\circ$, (b) $\alpha_n = 20^\circ$, (c) $\alpha_n = 25^\circ$, and (d) $\alpha_n = 35^\circ$

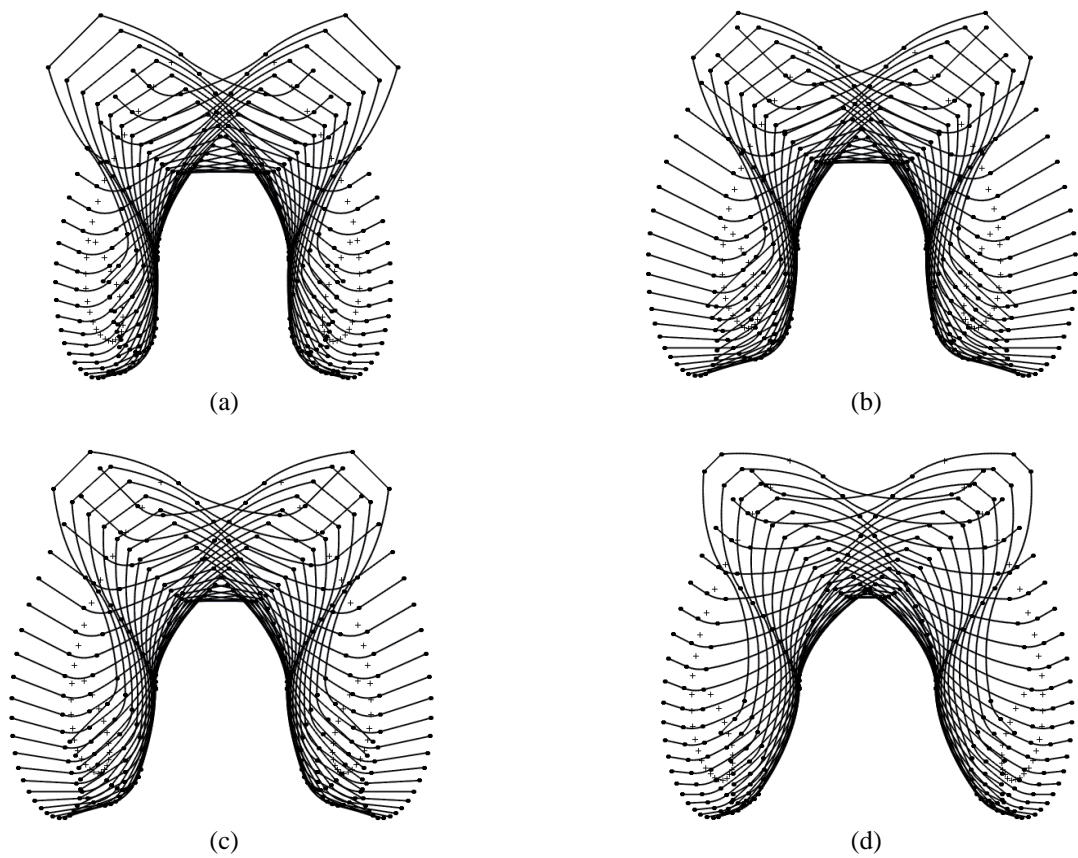


Figure 13. Cycloid tooth geometry for 14 teeth: (a) $R = 15$ mm, (b) $R = 12$ mm, (c) $R = 9$ mm, and (d) $R = 6$ mm

The two-dimensional shapes of the gear tooth profiles were constructed using SolidWorks software for comparative analysis of the findings [27]. The types examined include the involute profile, cycloidal profile, and modified tooth profile.

Different cutters were used to produce different types of tooth cross-sections. The teeth of the shaper cutter are a combination of epicycloid and involute curves, as demonstrated in Figure 14, formed by a straight line and a cycloid curve that is perpendicular to the oblique line and above the tool's pitch line. This design effectively prevents the gear teeth from rubbing against one another, which is essential for reducing or eliminating interference. Figure 14 presents the profile deviations resulting from variations in the pressure angles and rolling radius R . The selected R was 15 mm, 12 mm, and 9 mm. It is shown that the slope deviation of the gear tooth is positive when the material in the profile is increased closer to the tooth tip, in relation to the tooth design.

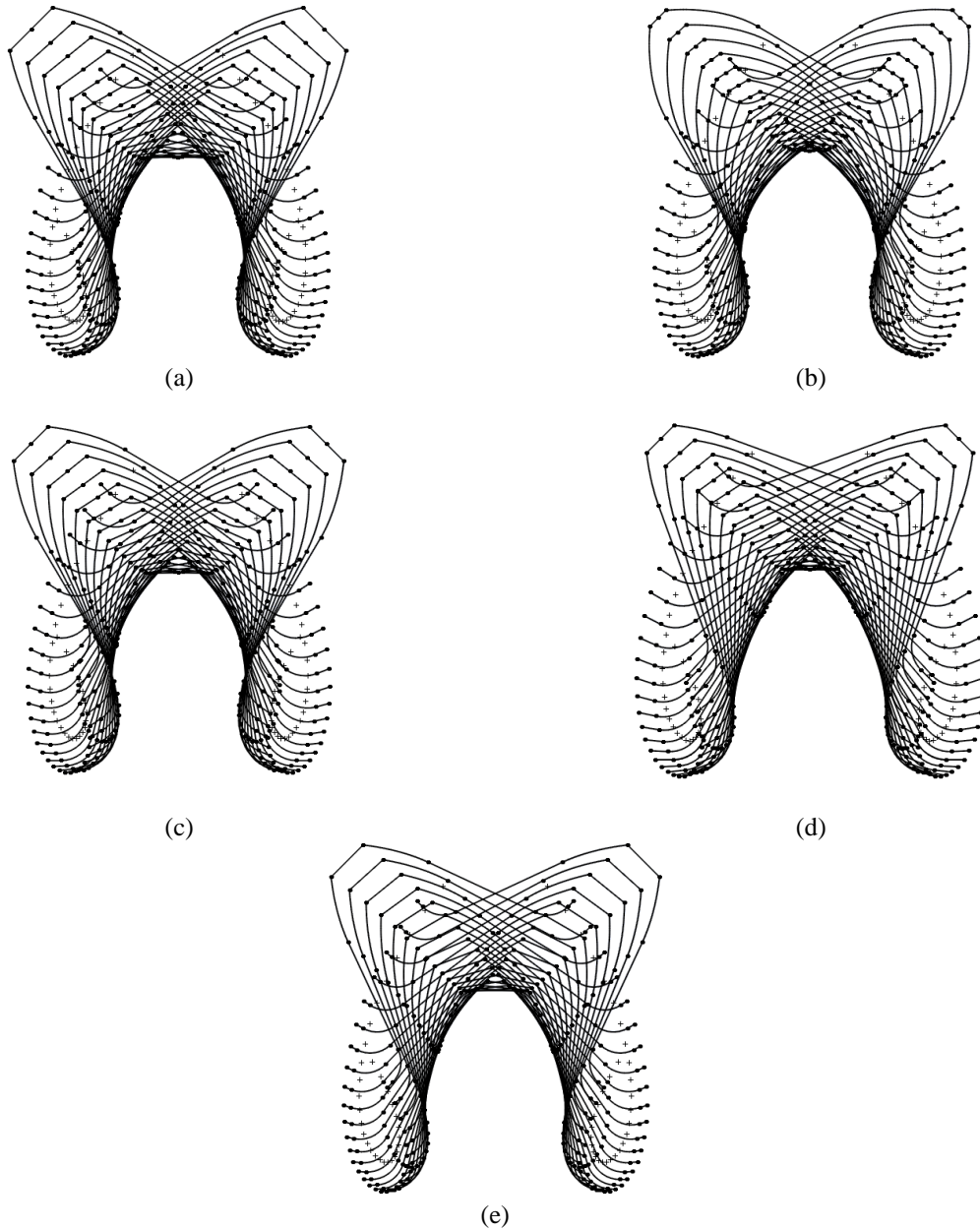


Figure 14. Modifications of involute-epicycloidal teeth geometry for 14 teeth: (a) $\alpha_n = 14.5^\circ$ and $R = 12$ mm, (b) $\alpha_n = 14.5^\circ$ and $R = 6$ mm, (c) $\alpha_n = 14.5^\circ$ and $R = 9$ mm, (d) $\alpha_n = 25^\circ$ and $R = 9$ mm, and (e) $\alpha_n = 20^\circ$ and $R = 9$ mm

Tables 1 and 2 present the thickness values obtained from the create-to-order samples for involute and cycloidal profiles, demonstrating the influence of several design parameters, such as pressure angles and roller radius, on the thickness of the tooth to mitigate excessive root stress. The findings indicate that the most important design elements for controlling tooth thickness in involute gears (which could increase by approximately 29.53%) and cycloidal gears (which could increase by 36.89%) are the angle of pressure and the rolling generating circle, respectively. This information is clearly shown in Figures 15 and 16. The thickness of the tooth increases with a higher pressure angle; conversely, it decreases as the rolling radius decreases, assuming that the normal module and the number of teeth remain constant at the same gear size. An analysis of these figures reveals a notable improvement in thickness. The study's most unexpected findings pertain to the improvement of bending strength achieved through the optimization of the pressure angle while minimizing the radius of the roller-generating circle.

Table 1. Tooth thickness (in mm) for different normal pressure angles for $m_n = 7$ mm and $Z = 14$ teeth

Cases	α_n	Tooth thickness (mm)
1	14.5°	11.17
2	20°	11.61
3	25°	12.63
4	35°	15.85

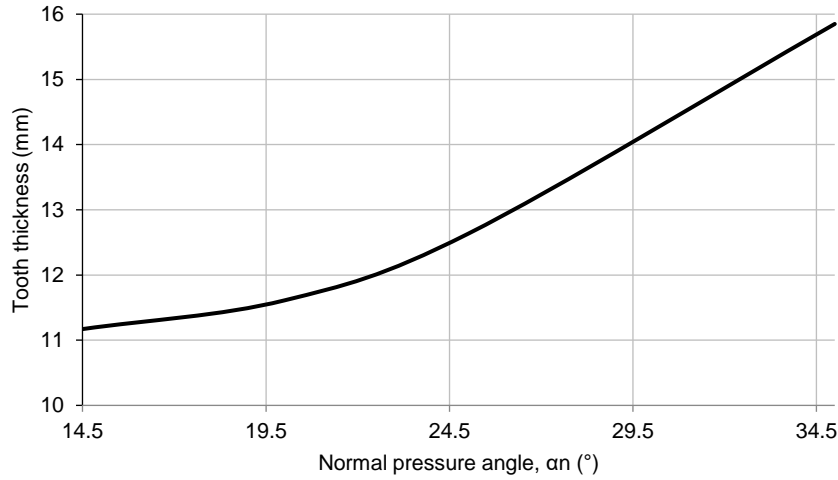


Figure 15. Relationship between normal pressure angle and teeth thickness

Table 2. Tooth thickness (in mm) for different cycloid teeth profiles for $m_n = 7$ mm and $Z = 14$ teeth

Cases	R (mm)	Tooth thickness (mm)
1	15	11.51
2	12	12.13
3	9	14.30
4	6	18.24

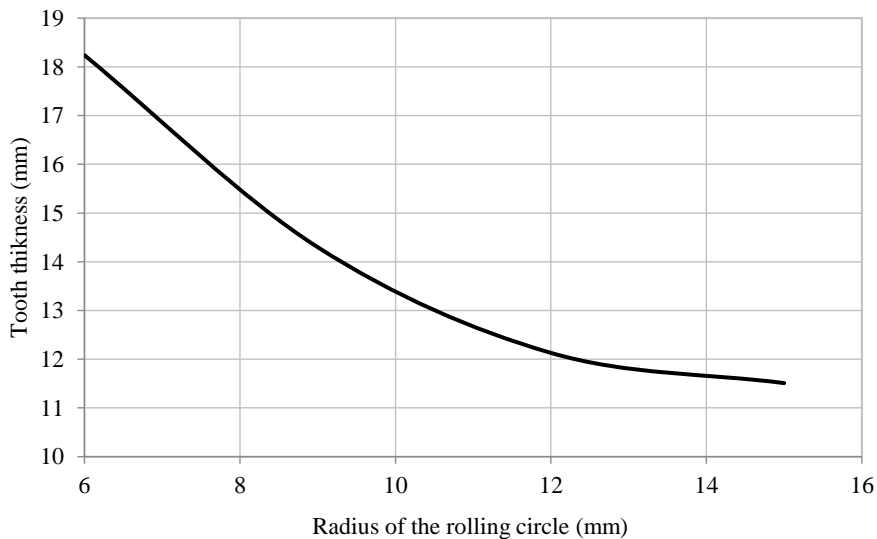


Figure 16. Relationship between the radius of the rolling circle and teeth thickness

In gear theory, helical gears are defined as a series of spur gears arranged at an angle equal to or exceeding that of a helix [28]. An appropriate screw motion parameter was used to generate the surface of the helical teeth, as illustrated in Figure 17, which includes several helical gear models with different helix angles. The connection between the screw parameter factor and the helix angle value at the pitch circle is inversely proportional, as shown in Figures 17 and 18. The proposed modification to the gear teeth employed in this study is demonstrated in Figure 17(e). Furthermore, when the helix angle is close to zero, the helical face width goes straight under small thrust loads (Figure 18). As the helix angle

increases, the thrust force grows, and the helical face width also becomes more spiral. Another benefit of the present work is the ability to alter the tooth profile to enhance thrust force. The optimal approach for reducing transmission error involves minimizing interference by reducing the common normal distance between tangent points.

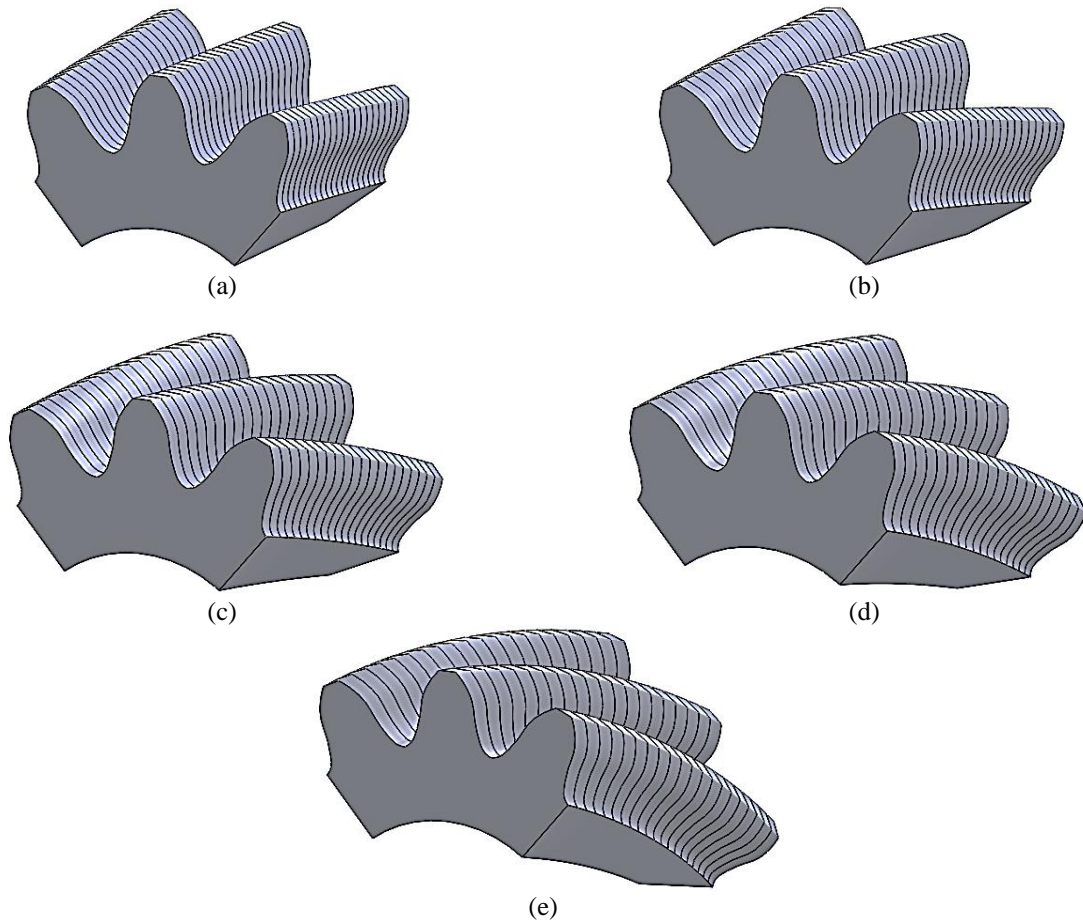


Figure 17. Helical gear models consisting of epi-involute-hypocycloidal teeth profile at $m_n = 7$ mm, $\alpha_n = 14.5^\circ$, $Z = 14$ teeth, and $R = 9$ mm with different helix angles of (a) $\beta = 15^\circ$, (b) $\beta = 22.5^\circ$, (c) $\beta = 30^\circ$, (d) $\beta = 37.5^\circ$, and (e) $\beta = 45^\circ$

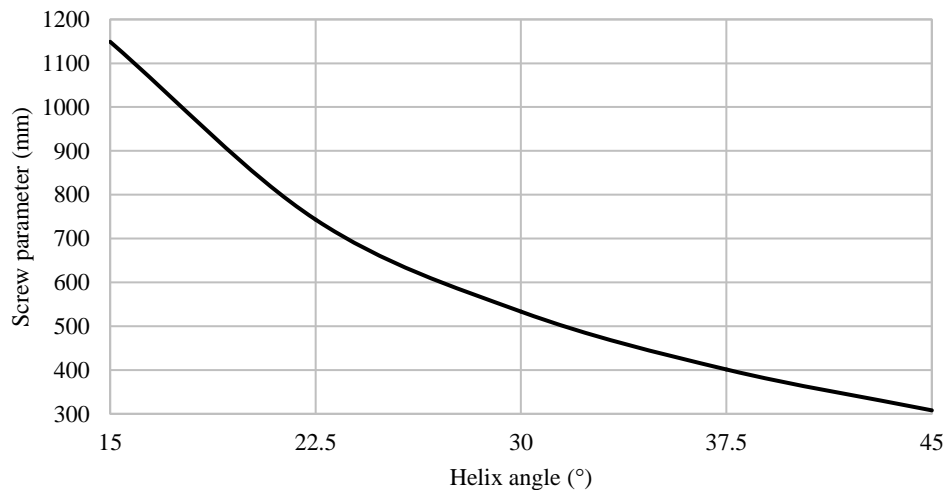


Figure 18. Relationship between helix angle and screw parameter

For comparing the results of contact and bending stresses, three cases of gear teeth profiles were examined. The first case is an involute teeth profile, the second case is a cycloidal tooth profile, and the third case is a modified tooth (epicycloid involute-hypocycloid teeth profile). Table 3 presents the various design parameters of mating non-parallel helical gears for all profiles. The material used in the evaluation is steel with Young's modulus of 207 GPa and a Poisson's ratio of 0.3. A constant power transmission of 20.0 kW at 1,440.0 rpm was applied across all models. Finite element analysis was conducted using ANSYS 2019 software to estimate the stress values [29], [30], and [31].

Table 3. Specifications of gear teeth

Cases	Normal module, m_n (mm)	Normal pressure angle, α_n (°)	Rolling circle radius, R (mm)	Helix angle, β (°)	Face width, F (mm)	No. of teeth
1	7	14.5	-	45	40	14
2	7	-	9	45	40	14
3	7	14.5	9	45	40	14

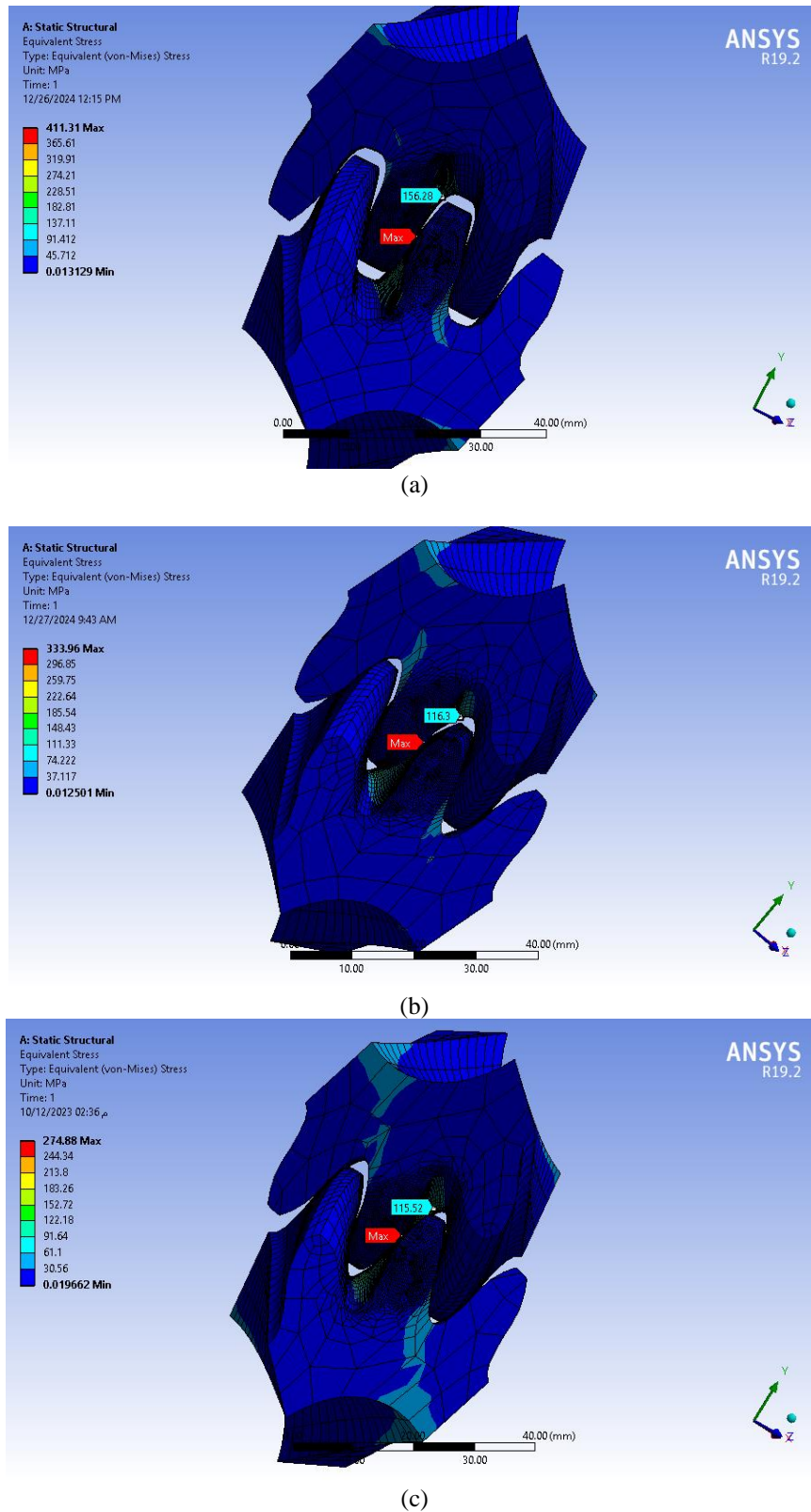


Figure 19. Von Mises criterion in non-parallel helical gears for (a) an involute gear, (b) a cycloidal gear, and (c) a combined gear

Table 4. Maximum criterion values

Cases	Contact stresses (MPa)	Bending stresses (MPa)
1	411.31	156.28
2	333.96	116.30
3	274.88	115.52

The models were configured to meet the boundary criteria. The mesh size of the gear tooth element improved gradually by increasing the mesh density. This section of the stress analysis aims to examine the contact and bending stresses in three instances of non-parallel helical gear drives, which are produced by an involute profile, a cycloid profile, and a modified tooth profile, as shown in Table 3. Figures 19(a), (b), and (c) present the results of the von Mises criteria for the involute, cycloidal, and modified tooth profiles, respectively, as analyzed using the ANSYS Workbench package. The results demonstrate a three-tooth model comprising three cases, each exhibiting a point of maximum contact stress located at the pitch region between the mated helical teeth, along with bending stress observed at the tooth root fillet region. Although the maximum stress value occurs at the pitch point, which can lead to scuffing and pitting, the bending stress significantly contributes to fractures in the gear field. This ultimately results in a jump in the gearbox drive, potentially leading to system failure. Table 4 presents the contact and bending stresses for all cases, indicating the highest values for the involute helical gear. Subsequently, the stress values decrease with a change in the teeth profile to the cycloid helical gear, followed by an increase observed with the compound helical teeth surface.



Figure 20. Relationship between cases of helical gears and contact stresses

In comparison to cases 1 and 2, the contact stress value for modification case 3 (274.88 MPa) is lower (see Figure 20). When compared to involute and cycloid helical teeth profiles, the compound-modified helical teeth profile achieved enhancements of approximately 33.169% and 17.690%, respectively. Regarding bending stress in this study, the involute tooth profile exhibits the worst case in thickness at the tooth root region. Figure 21 indicates that the bending stress values for the two usual examples are 156.28 MPa and 116.30 MPa, respectively. However, when using the modified helical tooth profile, the bending stress value is 152.52 MPa. The improvement percentages are 26.081% and 0.670% when compared to the involute and cycloid helical tooth profiles, respectively. The relationship between the cycloid helical teeth and the modified compounded helical teeth is nearly equivalent, as the utilized cutters possess identical cycloid curve dimensions, resulting in a congruent hypocycloid curve and matching tooth thicknesses. The decrease in contact and bending stresses is attributed to the interaction of the three compounded curves (epicycloidal, involute, and hypocycloidal), which results in a greater tooth thickness compared to the other helical gear cases 1 and 2. The modifications to the helical tooth gear components influence the configuration of the global stiffness matrix, leading to reduced induced stresses inside the gearbox unit.

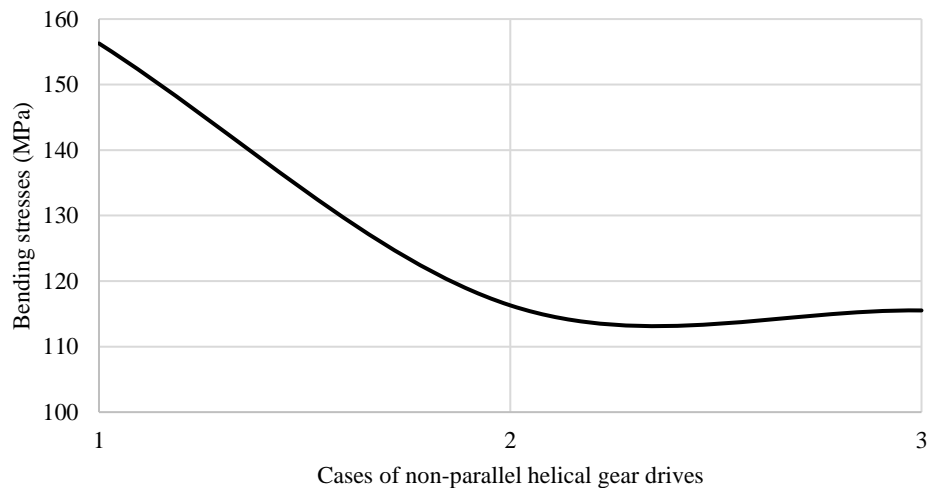


Figure 21. Relationship between cases of helical gears and bending stresses

6. CONCLUSION

The developed design and computer software for the creation of the combined involute-cycloidal teeth profile have successfully been applied. The conjugation of the gear tooth profile with profile modifications is accomplished by applying the modified cutter in the normal section. The main parts of the new method were generated automatically in the cross-section of the teeth by using the equations for gear teeth surfaces. The intersection points of the tooth profiles were obtained from the envelope of the family of rack-cutter shapes. The boundary conditions prevented the accuracy loss associated with developing solid models using CAD computer software. For the same design parameters, the epicycloid-involute-hypocycloidal non-parallel helical gear exhibited lower contact and bending stresses than other non-parallel helical gear profiles. Contact and bending stresses decreased by 33.169% and 26.08% compared to the standard involute profile, respectively. The reduction in contact and bending stresses was approximately 17.69% and 0.67% when compared to the cycloidal profile, respectively. Using the combination of curves (epicycloidal, involute, and hypocycloidal) in one tooth leads to an increase in the contact area. This, in turn, enhances the ability of the gears to withstand higher loads and prolongs their lifespan.

ACKNOWLEDGEMENT

The authors would like to express their sincere gratitude to all staff members of the Mechanical Engineering Department at the College of Engineering, University of Baghdad, for their cooperation and support during the preparation of this work.

CONFLICT OF INTEREST

The authors declare that they have no known competing financial interests or personal relationships that could have appeared to influence the work reported in this paper.

AUTHORS CONTRIBUTION

Mohammed Abdulaal Kadhim: Writing - original draft, Validation, Methodology.

Mohammad Qasim Abdullah: Review and editing, Validation, Methodology.

REFERENCES

- [1] F. B. Oswald, "Influence of gear design on gearbox radiated noise," *Journal of Gear Technology*, vol. 15, no. 1, pp. 10-15, 1998.
- [2] F. L. Litvin, Q. Lian, and A. L. Kapelevich, "Asymmetric modified spur gear drives: reduction of noise, localization of contact, simulation of meshing and stress analysis," *Computer Methods In Applied Mechanics and Engineering*, vol. 188, no. 1-3, pp. 363-390, 2000. [https://doi.org/10.1016/S0045-7825\(99\)00161-9](https://doi.org/10.1016/S0045-7825(99)00161-9)
- [3] R. M. Kumar, Studies on cycloidal gears made of isotropic and orthotropic materials, PhD thesis, Department of Mechanical Engineering, Bharathiar University, 2003.
- [4] S. Cănanău, "3D contact stress analysis for spur gears," in *National Tribology Conference*, vol. 24, pp. 349-351, 2003.
- [5] A. Kapelevich, "Direct design of asymmetric gears," in *Proceedings of MPT2009-Sendai JSME International Conference on Motion and Power Transmissions*, Matsushima Isles Resort, Japan, pp. 1-5, 2009.
- [6] K. Farhangdoost, and H. Heirani, "Contact stress on the surface of gear teeth with different profile," *International Journal of Mechanical and Mechatronics Engineering*, vol. 4, no. 8, pp. 649-656, 2010.

- [7] M. Q. Abdullah, and M. J. Jweeg, "Analytical solution of bending stress equation for symmetric and asymmetric involute gear teeth shapes with and without profile correction," *Journal correction, Innovative Systems Design and Engineering*, vol. 3, no. 6, pp. 19-33, 2012.
- [8] M. Q. Abdullah, and M. A. Kadum, "Stress concentration factor analysis of helical gear drives with asymmetric teeth profiles," *Journal of Engineering*, vol. 24, no. 5, pp. 14-28, 2018.
- [9] A. Miltenović, and M. Banić, "Thermal analysis of a crossed helical gearbox using FEM," *Transactions of FAMENA*, vol. 44, no. 1, pp. 67-78, 2020.
- [10] L. Becker, C. Kirchhoff, P. Tenberge, and D. Vill, "Extension of geometry and investigation of deformation on crossed helical gears to increase load capacity and performance," *Trans Motauto World*, vol. 7, no. 2, pp. 42-46, 2022.
- [11] J. Wu, P. Wei, C. Zhu, P. Zhang, and H. Liu, "Development and application of high strength gears," *The International Journal of Advanced Manufacturing Technology*, vol. 32, no. 9, p. 3123–3148, 2024.
- [12] M. Temirkhan, H. B. Tariq, K. Kaloudis, C. Kalligeros, V. Spitas, and C. Spitas, "Parametric quasi-static study of the effect of misalignments on the path of contact, transmission error, and contact pressure of crowned spur and helical gear teeth using a novel rapidly convergent method," *Applied Sciences*, vol. 12, no. 19, p. 10067, 2022.
- [13] J. Smith, *Gear noise and vibration*, New York: 270 Madison Avenue, New York, NY 10016. ISBN: 0-8247-4129-3, 2003.
- [14] X. Li, H. Yang, W. Niu, R. Guo, and L. Sun, "Investigation on tooth surface wear of cycloid drives considering tooth profile modifications," *Lubricants*, vol. 11, no. 8, p. 323, 2024.
- [15] S. Jyothirmai, R. Ramesh, T. Swarnalatha, and D. Renuka, "A finite element approach to bending, contact and fatigue stress distribution in helical gear systems," *Procedia Materials Science*, vol. 6, pp. 907-918, 2014.
- [16] D. Zorko, J. Duhovnik, and J. Tavčar, "Tooth bending strength of gears with a progressive curved path of contact," *The Japan Society of Mechanical Engineers*, vol. 8, no. 4, pp. 1037-1058, 2021.
- [17] J. I. Pedrero, M. B. Sánchez, M. Pleguezuelos, and A. Fuentes-Aznar, "Analysis of the tooth-root stress of external spur gears with high effective contact ratio," *Mechanism and Machine Theory*, vol. 203, p. 105813, 2024.
- [18] Y. Yan, H. Guo, J. Gu, N. Zhao, and L. Liu, "Computerized generation, deviation correction and rapid tooth contact analysis of helical face gear," *Mechanism and Machine Theory*, vol. 203, p. 105789, 2024.
- [19] C. Robert, M. Juvinal, and M. KURT, *Fundamentals of machine component design*, John Wiley & Sons, 2021.
- [20] S. P. Radzevich, *Theory of gearing: kinematics, geometry, and synthesis*, CRC Press, 2022.
- [21] S. P. Radzevich, "Poor understanding of the scientific theory of gearing by the majority of gear scientists and engineers," *Novikov/Conformal Gearing: Scientific Theory and Practice*, vol. 15, pp. 193-214, 2022.
- [22] C. Jia, Q. He, J. Xiao, and H. Dong, "Design and analysis of novel non-involute cylindrical gears with a curved path of contact," *Mathematics*, vol. 10, no. 22, p. 4290, 2022.
- [23] E. Trubachev, T. Savelieva, and T. Pushkareva, "Practice of design and production of worm gears with localized contact," *Mechanisms and Machine Science*, vol. 51, pp. 327-343, 2018.
- [24] D. Babichev, and M. Storchak, "Quality characteristics of gearing," *Mechanisms and Machine Science*, vol. 51, p. 73–90, 2018.
- [25] M. Abdulaal, and M. Q. Abdulah, "Mathematical model and generation analysis for crossed helical gear system," *World Journal of Engineering*, 2024.
- [26] Z. Sun, J. Tang, S. Chen, X. Tan, X. Tao, Z. Hu et al., "Analytical method for gear body-induced tooth deflections of hybrid metal-composite gears," *International Journal of Mechanical Sciences*, vol. 261, p. 108701, 2024.
- [27] S. A. Afolalu, J. F. Kayode, B. Adaramola, S. I. Monye, O. M. Ikumapayi, L. Oloyede and e. al., "The design and simulation of helical gear," in *2024 International Conference on Science, Engineering and Business for Driving Sustainable Development Goals (SEB4SDG)*, pp. 1-12, 2024.
- [28] S. P. Radzevich, and D. W. Dudley, *Handbook of practical gear design*, USA: CRC press, ISBN-1-56676-218-9, 1994.
- [29] P. M. Ramachandra, S. Sutar, and G. M. Kumara, "Stress analysis of a gear using photoelastic method and Finite element method," *Materials Today*, vol. 65, pp. 3820-3828, 2022.
- [30] A. A. Toman, and M. Q. Abdullah, "An analytical approach for predicting the fillet and contact stresses in symmetric and asymmetric spur gears under frictional mesh assumptions," *Results in Engineering*, p. 102391, 2024.
- [31] W. Hussein, and M. Q. Abdullah, "High-contact ratio spur gears with conformal contact and reduced sliding," *Results in Engineering*, vol. 14, p. 100412, 2022.